Research Article | Vol. 28, No. 10 / 11 May 2020 / Optics Express 14405
Optics EXPRESS

Optical lock-in camera for gravitational wave detectors

HUY TUONG CAO,[1,2] DANIEL D. BROWN,[1,2,*] PETER J. VEITCH,[1,2] AND DAVID J. OTTAWAY[1,2]

[1]Department of Physics and The Institute of Photonics and Advanced Sensing (IPAS), University of Adelaide, SA, 5005, Australia
[2]OzGrav, Australian Research Council Centre of Excellence for Gravitational Wave Discovery, Australia
*daniel.d.brown@adelaide.edu.au

Abstract: Knowledge of the intensity and phase profiles of spectral components in a coherent optical field is critical for a wide range of high-precision optical applications. One of these is interferometric gravitational wave detectors, which rely on the optical beats between these fields for precise control of the experiment. Here we describe an *optical lock-in camera* and show that it can be used to record optical beats at MHz or greater frequencies with higher spatial and temporal resolution than previously possible. This improvement is achieved using a Pockels cell as a fast optical switch to transform each pixel on a sCMOS array into an optical lock-in amplifier. We demonstrate that the optical lock-in camera can record fields with 2 Mpx resolution at 10 Hz with a sensitivity of -62 dBc when averaged over 2s.

1. Introduction

The detection of gravitational waves (GW) [1] has ushered in a new era of gravitational and multi-messenger astronomy. Improving the sensitivity of current and next-generation detectors will ensure that they fulfill their potential to observe this exciting new window on the universe. Reaching these goals however will require a significant reduction in quantum noise, which can be achieved by increasing both the optical power stored within the interferometer and the use of squeezed light [2,3]. To maximize the benefit from these upgrades it is essential that precise control of the circulating optical fields within the interferometer is maintained. This will require sensors that can measure the spatial variations in magnitude and phase of the various circulating fields within the interferometer.

Optical heterodyne techniques are used extensively throughout ground-based GW detectors to generate *error signals* which control the positions and alignments of the suspended optics [4–7]. These systems use radio-frequency (RF) phase-modulated sidebands that are imposed on a carrier field and resonate within the different optical cavities of the interferometer. The weakly modulated RF beat-notes are demodulated at various single- and quad-element photodiodes to produce error signals, but with limited spatial resolution.

Wavefront distortions from static surface errors in the optics or thermal aberrations due to optical absorption in the substrates or small highly-absorbing defects in coatings can introduce significant time-dependent offsets in error signal set points and increased noise couplings [8]. This is because sidebands experience different resonant conditions within the interferometer and becoming distorted relative to each other, resulting in poor spatial overlap. This imbalance leads to a degradation of the error signals and the performance of the control systems. Thus, detailed knowledge of all the carrier and sideband fields is required to fully understand control sensing issues and design adequate solutions for increasing interferometer sensitivity and robustness.

One tool that had been previously developed to study the complex amplitude of various spectral components was the *phase camera* [9], which was first used to measure the mode structure of the power-recycling cavity and the output of Initial LIGO [10,11]. This technique is currently

#384754 https://doi.org/10.1364/OE.384754
Journal © 2020 Received 10 Jan 2020; revised 28 Mar 2020; accepted 9 Apr 2020; published 28 Apr 2020

Optics EXPRESS

used in the Advanced Virgo detector to assist its thermal compensation system (TCS) to maintain the control of its marginally-stable power-recycling cavity, which is particularly susceptible to thermally-induced distortion [12]. This sensing scheme combines the interferometer fields with a reference field to generate spatially dependent heterodyne beats. These phase cameras generate 2D maps by actively scanning this combined field over a small photodiode using galvanometer or tip-tilt mirrors. The signal from the photodiode is then demodulated at the beat frequency of interest to generate the magnitude and phase maps. The maximum achievable spatial and temporal resolution is limited by the mechanical resonances of the scanner and the size of the photodiode. Additionally, the scanning can cause mechanical vibrations and time-varying scattering which introduces excess noise to the gravitational wave channel and thereby limits the observing range of the increasingly sensitive GW detectors [13–15].

In this paper we describe and demonstrate an alternative phase camera approach that has no moving parts. Our approach uses a Pockels cell as a fast optical switch which transforms the array of pixels of a scientific CMOS sensor into a parallel array of optical lock-in amplifiers demodulating at frequencies up to 100 MHz. The advances in CMOS sensors over the last decade has allows us to reconstruct the magnitude and phase maps of individual spectral component in an optical field with high sensitivity and both high spatial and temporal sampling rates.

We begin with an overview of the operating principle of the optical lock-in phase camera. The experimental realization of the phase camera is outlined in Sec. (3). Measured intensity and phase maps are compared with the predictions of a numerical model of the test system. We also demonstrate that the sensitivity is shot-noise limited and can thus be improved simply by averaging in Sec. 4.

2. Principle of operation

To illustrate the operation of the new camera we consider a linearly polarized beam consisting of two components: a reference field $E_r(x,y)\exp[i(\omega_r t + \varphi_r(x,y))]$ and a signal field $E_s(x,y)\exp[i(\omega_s t + \varphi_s(x,y))]$. We wish to determine the spatial distribution of the magnitude and phase of the signal field relative to a reference field, which is phase-locked to and frequency offset from the reference field. This frequency offset in gravitational wave detectors is typically in the 1–100 MHz region. Measuring this composite field using a photodetector would yield a voltage:

$$\begin{aligned} V(x,y) \propto\ & E_r(x,y)^2 + E_s(x,y)^2 \\ & + 2E_r(x,y)E_s(x,y)\sin(\Omega t + \varphi(x,y)) \end{aligned} \tag{1}$$

where $\Omega = \omega_r - \omega_s$ and $\varphi(x,y) = \varphi_r(x,y) - \varphi_s(x,y)$. However, the frequency of the heterodyne beat is much larger than the bandwidth of a typical pixelated camera and would not be measurable. Thus, we synchronously amplitude modulate the field incident on each pixel as shown in Fig. 1. In this example, a square-wave amplitude modulation is applied to the beam at a frequency Ω, with a phase $\phi = \varphi$, which yields the largest signal. For in-phase modulation, the pixel detector observes intensities that are greater than the unmodulated intensity, resulting in a DC output $(V_r + V_s)/2 + \delta V$, where the $V_{r/s}$ are due to the $E_{r/s}(x,y)^2$ terms in Eq. (1) and δV is due to the RMS average of the $E_r(x,y)E_s(x,y)$ term. Similarly, for the modulation phase $\phi = \varphi + \pi$, the pixel observes intensities that are less than the unmodulated intensity, $(V_r + V_s)/2 - \delta V$. Subtraction of these provides $2\delta V \propto E_r(x,y)E_s(x,y)$.

The optimum demodulation phase ϕ is not known a priori. Thus we record four camera images, V_ϕ at $\phi = \{0, \pi/2, \pi, 3\pi/2\}$ for example. Combining these images yields the magnitude and phase of the heterodyne beat:

$$\mathbf{I} \equiv V_0 - V_\pi \tag{2}$$

$$\mathbf{Q} \equiv V_{3\pi/2} - V_{\pi/2} \tag{3}$$

Optics EXPRESS

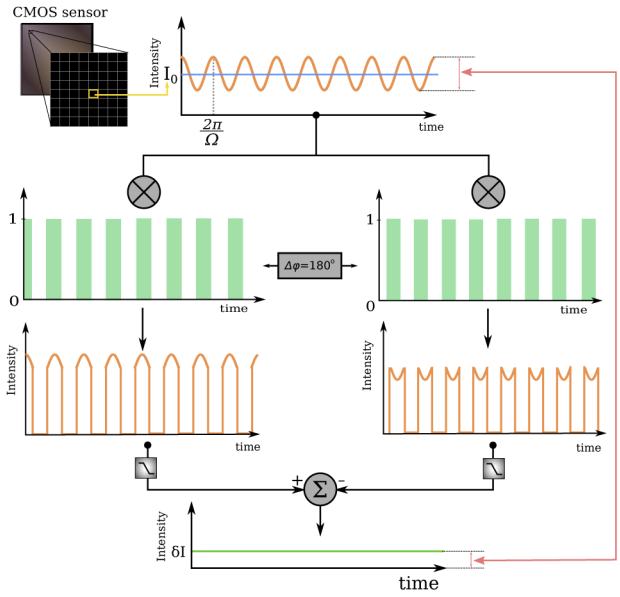

Fig. 1. The operation of the new camera can be visualized by considering the beat signal measured by a single pixel. Synchronous intensity modulation of the incident light field at frequency Ω allows the pixel to extract a DC signal that is a function of the magnitude and phase of the beat.

$$|E_r(x,y)E_s(x,y)| \propto \sqrt{(\mathbf{I})^2 + (\mathbf{Q})^2}, \tag{4}$$

$$\varphi = \arctan\left(-\frac{\mathbf{Q}}{\mathbf{I}}\right). \tag{5}$$

where we refer to **I** and **Q** as the "in-phase" and "quadrature" signals. The heterodyne beat has thus been demodulated to baseband by the optical switching, and hence the analogy to a lock-in amplifier.

A schematic of a practical realization is shown in Fig. 2. The composite beam is first filtered using a polarizer and then circularly polarized using a quarter-wave plate. It then passes through a Pockels cell (PC) driven with a half-wave voltage that switches the polarization of the beam between *s* and *p* linear polarization. The polarizer converts this polarization modulation into an amplitude modulation. Typical camera images and the result of processing using Eq. (4) and (5) are shown in Fig. 2.

The maximum image rate could in principle be doubled by recording both the transmitted and reflected beams simultaneously. In practice it is difficult to overlap the images from both cameras to enable an accurate subtraction. Additional differential effects, such as variation in the responsivity of the sCMOS arrays and aberrations in the polarizing beamsplitter, also reduce the performance in the dual camera operation.

The maximum power the optical lock-in camera can handle is limited by the camera pixels becoming saturated. The minimum power is limited by several factors that depend on the use case: frame rate, if you run at 40fps then you can only expose for 25ms limiting the collected number of photons; the bandwidth required, if you have a stable or slowly varying signal field you can average the phase camera images for longer; resolution requirement, you could make the beam incident on the camera smaller for greater intensity per pixel and perform region of interest capturing, or pixel binning, sacrificing higher resolution images. Further details on calculating noise limits can be found in section 4.

Optics EXPRESS

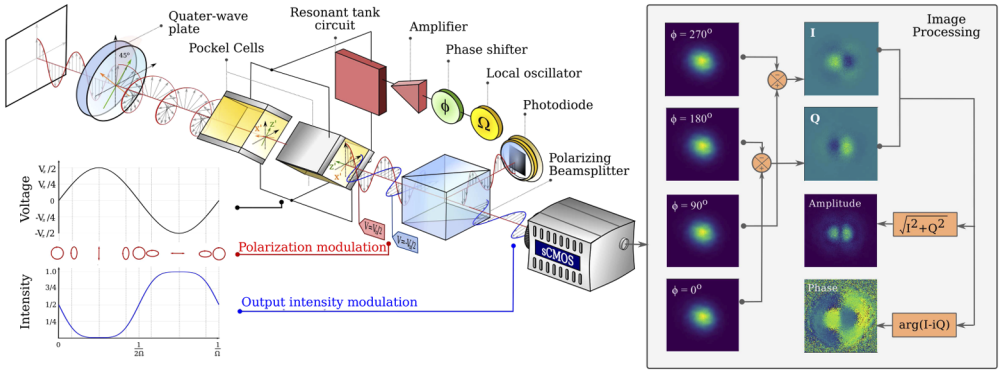

Fig. 2. A schematic layout of the new camera. The quarter-wave plate, Pockels cell and polarizing beamsplitter form an optical switch that intensity modulates the beam incident on the sCMOS camera. Spatially-resolved magnitude and phase maps of the heterodyne beat between a reference field and a signal field that is frequency shifted from a reference field is calculated using four camera images acquired with modulation phases separated by $\pi/2$.

3. Test setup

We follow the approach presented in [9] to demonstrate the operation and sensitivity of the optical lock-in camera. A schematic of the test system is shown in Fig. 3. It consists of two parts: a test field generator that produces a reference and signal field and the lock-in camera itself to image them. In this setup the reference field and signal field propagate along a common path. Thus environmental noises, such as vibrations, are common-mode between the two. In practice, when used in a gravitational wave detector this setup would be implemented to image and analyse the optical beat between the radio-frequency modulated sidebands that are used to control many of the interferometer degrees of freedoms.

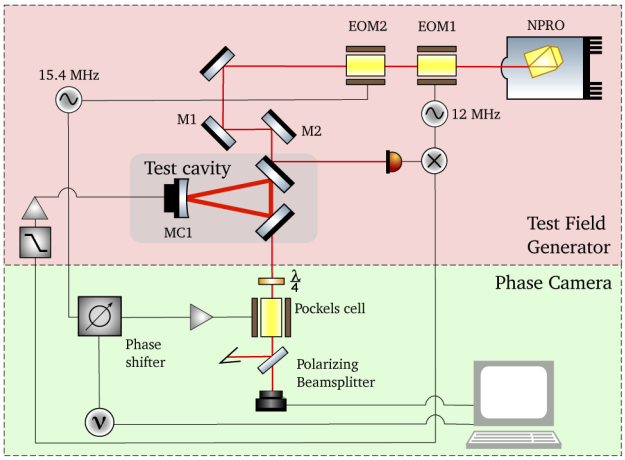

Fig. 3. Schematic of the optical system used to demonstrate the camera. The test field generator shown in the red box is used to produce a beam consisting of a reference and signal field.

The test field consists of a large-amplitude TEM_{00} mode and a higher-order mode of a high-finesse, ≈ 4000, ring cavity that has a free spectral range of 540 MHz. The TEM_{00} mode is produced by phase-locking a Nd:YAG NPRO to a TEM_{00} mode of the ring cavity using the

Optics EXPRESS

Pound-Drever-Hall technique [4] and the electro-optic phase modulator EOM1, approximately 20μW of power is transmitted through the cavity and incident on the phase camera.

Higher-order modes are excited in the cavity by misaligning the incident beam using M1 and M2 and phase-modulating the beam at the cavity offset frequency using EOM2. The odd number of mirrors in the ring cavity breaks the resonance degeneracy between odd- and even-parity optical modes due to the odd-parity modes accumulating an additional π phase shift during each round trip [16,17]. In our cavity, the TEM_{30} and TEM_{12} Hermite-Gauss modes resonate closest to the TEM_{00} mode, at offset frequencies of 15.7 MHz and 15.3 MHz respectively.

For the test described here, we chose to drive EOM2 at 15.4 MHz as it enabled the excitation of both modes. The beam emitted by the ring cavity therefore consists of a large-amplitude TEM_{00} reference field with frequency ω_r, and a smaller-amplitude TEM_{30} and TEM_{12} signal field oscillating mostly at the 15.4 MHz-shifted frequency, ω_s.

The performance of the camera is affected by the sCMOS properties. A high dynamic range, bit-depth, and linearity are crucial as we must subtract images to remove the offset due to the high power carrier. A high frame rate is also required as four frames are required to produce the intensity and phase images, and to allow averaging of shot noise, provided it does not result in an unacceptable reduction in dynamic range or spatial resolution.

In this work we use a Zyla 4.2 sCMOS camera, which has a sensor size of 2048x2048 pixels, a dynamic range of 89 dB, a 16-bit readout, a maximum frame rate of 100 fps and a quantum efficiency of 3–4% at 1064 nm. The camera window was anti-reflection coated for the 1064 nm. The rolling-frame shutter for this camera does not affect the measurement process as the demodulation phases for each pixel are still separated by $\pi/2$.

4. Results

Typical **I** and **Q** images and the result of a numerical simulation of the test-field generator using FINESSE[18] are shown in Fig. 4. In this case, the TEM_{30} mode is apparent in the Q demodulation while the TEM_{12} mode occurs mostly in the I demodulation. Only the two central maxima of the TEM_{30} mode are observed in this demonstration as the magnitude of the TEM_{00} reference field is much smaller at the location of the outer maxima.

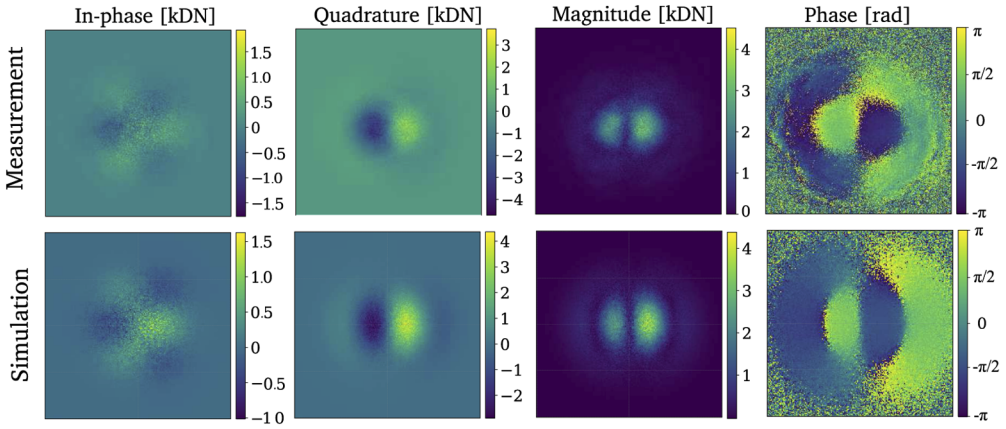

Fig. 4. Comparison between camera measurements and the predictions from a FINESSE simulation. The digitized pixel values are given in units of thousands of digital-numbers (kDN) and plotted using the false-color scale bars.

The FINESSE simulation used plausible misalignments and included shot noise to reproduce outputs of the optical system. For the simulation shown in Fig. 4, the ratio of the power in

Optics EXPRESS

higher-order mode to that in the TEM_{00} was 14% for the TEM_{30} and 8% for the TEM_{12} modes, and thus the magnitude is dominated by the TEM_{30} mode but the phase shows some influence of the weaker TEM_{12} mode, which degrades the spatial resolution we are able to demonstrate below.

The sensitivity of the optical lock-in camera was investigated by removing the 15.4 MHz modulation from EOM2 and recording frames with the demodulation phase alternating between 0 and π and studying the noise levels. Fig. 5(a) shows the noise present in pixels at varying distances from the center of the beam with the estimated shot noise from the TEM_{00} reference field. The excess noise seen in the figure is due to intensity noise present on an older NPRO laser that was used. A similar test was undertaken with a newer higher power NPRO manufactured by Lightwave (which was not available during the time the main cavity experiment was originally conducted) with the results shown in Fig. 6.

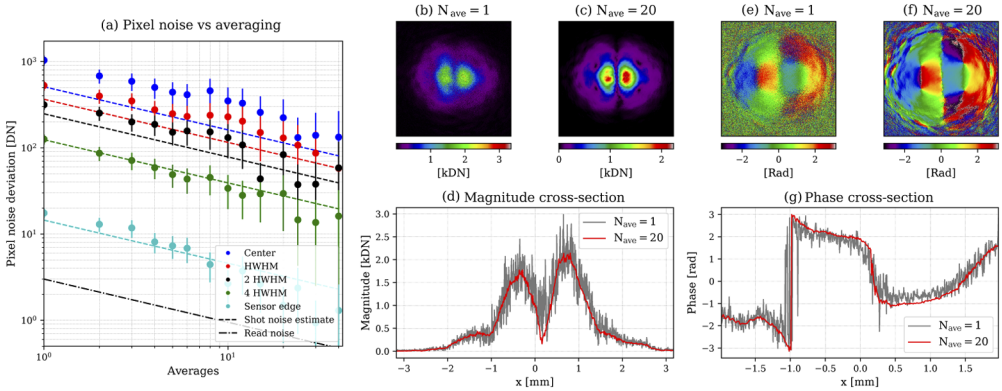

Fig. 5. (a) The measured noise and estimated shot noise present at varying distanced from the center of the beam. (b, c) Maps of the magnitude of the heterodyne beat for $N_{\text{ave}} = 1$ and $N_{\text{ave}} = 20$. (e,f) Maps of the phase of the heterodyne beat for $N_{\text{ave}} = 1$ and $N_{\text{ave}} = 20$. Images (e) and (h) were taken with 2×2 pixel binning. (d) Plots the magnitude variation along the center of (b) and (c). (g) Plots the Phase variation along the center of (e) and (f).

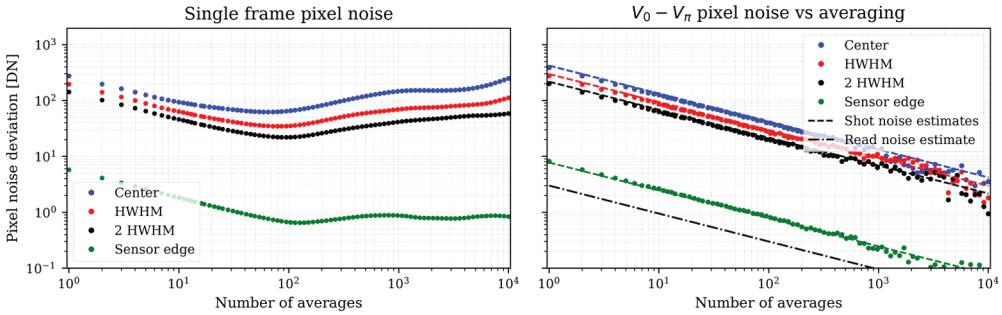

Fig. 6. Measured noise using a Lightwave NPRO with reduced amplitude noise. Plotted is the Allan deviance of 100k samples of pixel noise sampled at 20fps at various distances from the center of an incident gaussian beam. No RF modulation signal field is present. The left plot shows how a pixel averages over many samples, after 100 samples laser power drift causes large deviations. The right plot shows the noise present in the subtracted frames. Also shown are the read and shot noise estimates, showing we are limited by shot noise.

In this later test a beam of spot radius of $w = 3.3$mm with power of 45μW was incident on the camera, whose exposure time was $\tau = 1.5$ms. The power incident on a pixel near the center

Optics EXPRESS

of a Gaussian beam is $P\,\mathrm{erf}\left(\frac{h}{\sqrt{2}w}\right)^2$, where $h = 6 \cdot 10^{-6}$m is the pixel dimension. At 1064nm Andor does not specify the quantum efficiency, however from the trend of the plots it provides we can assume it is around $Q_E \approx 3\%$ to 4%. The camera outputs $N_{\mathrm{bits}} = 16$ bits per pixel and has a well depth of $W_d = 30000$ electrons. The shot-noise at the center of the reference field in the subtracted frames (assuming N_e is similar in both frames) in units of digital number (DN) is

$$K\sigma_{SN} = K\sqrt{2N_e} = K\sqrt{2\tau Q_E P\,\mathrm{erf}\left(\frac{h}{\sqrt{2}w}\right)^2 \frac{1064\mathrm{nm}}{hc}} \approx 460\text{–}520 \tag{6}$$

where N_e is the number of photo-electrons captured in the pixel, h planks constant, c the speed of light, and $K = \frac{2^{N_{\mathrm{bits}}}}{W_d}$, the conversion factor between photo-electrons and digital number. The uncertainty in Q_e, the sensor fill-factor, and the loss of power from the sensor window are unknown and largely limit how accurate we can predict the shot-noise limit. Comparing this to the read-noise which we estimate to be about $\sigma_{read} \approx 3$ DN, which appears to be white noise from studying dark frames, does not even limit the edge pixels. The sensor is cooled and the manufacturer states the dark noise is 0.1–0.9 electrons/second depending on the sensor temperature, which is negligible for short exposure times used here.

The improvement in sensitivity due to averaging was demonstrated by reinstating the 15.4 MHz modulation of EOM2 and recording twenty frames, each containing a sample of each of the four demodulation phases. The magnitude and phase of the beat with $N_{\mathrm{ave}} = 1$ and $N_{\mathrm{ave}} = 20$ are shown in Fig. 5(b) and (c), and (e) and (f) respectively. Averaging over 20 frames improves the signal-to-noise ratio in the maps as seen in Fig. 5(d) and (g). In addition to the averaging, pixel-binning can also be employed for further SNR improvements without sacrificing speed—as was used for the $N_{\mathrm{ave}} = 20$ cases above, where 2×2 binning was employed.

The minimum signal power detectable can be estimated from the ratio of the digital number (DN) noise on the large peaks in Fig. 5(d) to the DN of the reference field, which is $|E_r|^2 \approx 60$ kDN. The noise is measured to be ≈900 DN at the peak parts of the signal field, for the 20 averages and 2x2 binning our noise drops to $\sigma/(N_{\mathrm{bin}}\sqrt{N_{\mathrm{ave}}}) \approx 100$ DN, as measured. The quantity the phase camera measures is the optical beat $2|E_s||E_r| = \sigma$. We define the sensitivity as the signal power relative to the carrier, in dBc,

$$S = 10\log_{10}\left(\frac{|E_s|^2}{|E_r|^2}\right) \equiv 10\log_{10}\left(\left[\frac{2|E_s||E_r|}{2|E_r|^2}\right]^2\right) \equiv 10\log_{10}\left(\left[\frac{\sigma}{2|E_r|^2}\right]^2\right). \tag{7}$$

The single-shot sensitivity is measured as $10\log_{10}([0.9/(2 \cdot 60)]^2)$, after 20 averages and 2x2 binning we find $10\log_{10}\left([0.1/(2 \cdot 60)]^2\right) \approx -62$ dBc below the power in the reference field—a 12 dB improvement on that reported in [9]. We would expect this to improve by ≈ 3 dB if the NPRO with reduced intensity noise had been used.

We can also estimate the single-shot shot-noise limited sensitivity. Consider a pixel is using the full well-depth, $\sigma = K\sqrt{2W_d}$ and $|E_r|^2 = KW_d$, results in a sensitivity $10\log_{10}(1/(2W_d N_{\mathrm{bin}}^2 N_{\mathrm{ave}}))$, so a single-shot limit being −47.8 dBc. Thus, cameras with large pixel well-depths and $2^{N_{\mathrm{bits}}} \geq W_d$ to avoid quantisation errors when computing subtracted frames should be used for maximising the sensitivity of the optical lock-in camera.

The relatively poor signal-to-noise associated with the outer maxima of the TEM_{30} signal field is due to the small diameter of the TEM_{00} reference field in the test system. It could be improved by using a larger diameter reference field that is frequency-offset locked to the signal field, or by using a liquid crystal attenuator or spatial light modulator [19–21].

To analyze the output of phase cameras it will be important to extract the relative phase of the higher order modes in a beam. Figure 7 shows how the modal content extracted from the in-phase and quadrature images varies with demodulation phase. The amount of each mode is

Optics EXPRESS

inferred by performing a least-squares fit of the TEM_{30} and TEM_{12} with the data, this is done for each demodulation phase measured. We can see that the TEM_{12} mode is out-of-phase with the carrier at 85° and the TEM_{30} at 135°—this phase relationship agrees well with that predicted by the FINESSE model.

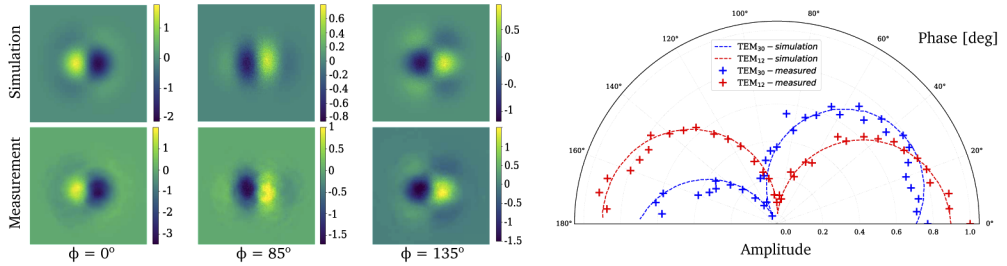

Fig. 7. The measured and simulated demodulated signal mode content. $\phi = 0^o, 85^o, 135^o$ are shown on the left with the corresponding simulation showing the individual modes. The data and model have been scale normalized.

5. Conclusion

In this work we have introduced a new type of phase camera, the optical lock-in camera, and demonstrated its ability to produce high spatial resolution maps of the phase and intensity of a coherent light field. This is achieved with a higher acquisition rate and resolution than previous phase camera implementations. The camera is both compact and does not rely on any mechanically moving parts, thus reducing potential scattered light issues and should enable operation during scientific observations in gravitational wave interferometers. Initial tests of the optical lock-in camera during the O3 commissioning break at LIGO Hanford [22,23] showed no additional limiting noise sources from the use of the phase camera.

The phase and intensity of a specific frequency component of a beam is imaged by creating a heterodyne beat with a reference field and synchronously amplitude modulating it. The key element is the Pockels cell which acts as a fast optical switch to provide the amplitude modulation. By switching over the entire field optically, rather than electronically, and imaging with a sCMOS array, each pixel can behave as an optical lock-in amplifier demodulating at RF frequencies.

The results of our proof-of-principle measurements are in excellent agreement with the predictions of a theoretical FINESSE model in our test system. We also demonstrate that the sensitivity is limited by shot-noise and can be improved by simple temporal or spatial averaging, resulting in a noise floor of -62 dBc from data recorded in 2s. The performance can be easily improved by using faster or more sensitive cameras, such as InGaAs arrays which can achieve >100 Hz frame rates, or by sacrificing spatial resolution for faster acquisition rates on dense sCMOS arrays, by region-of-interest extraction or pixel-binning.

The additional information provided by these phase cameras should enable better diagnostics of high spatial frequency effects within an interferometer. This will provide a new tool for improving both their duty-cycle and sensitivity. We believe this will be particularly important for the thermal compensation systems as ever increasing stored optical power is used in current and future generations of detectors. This work paves the way now for testing these devices in practice at operational gravitational wave interferometers.

Funding

ARC (CE170100004, DP150103359).

Optics EXPRESS

Disclosures

The authors declare no conflicts of interest.

References

1. B. P. Abbott, "Gw150914: The advanced ligo detectors in the era of first discoveries," Phys. Rev. Lett. **116**(13), 131103 (2016).
2. P. Kwee, J. Miller, T. Isogai, L. Barsotti, and M. J. Evans, "Decoherence and degradation of squeezed states in quantum filter cavities," Phys. Rev. D **90**(6), 062006 (2014).
3. D. Töyrä, D. D. Brown, M. Davis, S. Song, A. Wormald, J. Harms, H. Miao, and A. Freise, "Multi-spatial-mode effects in squeezed-light-enhanced interferometric gravitational wave detectors," Phys. Rev. D **96**(2), 022006 (2017).
4. E. D. Black, "An introduction to pound-drever-hall laser frequency stabilization," Am. J. Phys. **69**(1), 79–87 (2001).
5. P. Fritschel, N. Mavalvala, D. Shoemaker, D. Sigg, M. Zucker, and G. González, "Alignment of an interferometric gravitational wave detector," Appl. Opt. **37**(28), 6734–6747 (1998).
6. G. Mueller, Q. ze Shu, R. Adhikari, D. B. Tanner, D. Reitze, D. Sigg, N. Mavalvala, and J. Camp, "Determination and optimization of mode matching into optical cavities by heterodyne detection," Opt. Lett. **25**(4), 266–268 (2000).
7. K. Agatsuma, M. van Beuzekom, L. van der Schaaf, and J. van den Brand, "Phase camera experiment for advanced virgo," Nucl. Instrum. Methods Phys. Res., Sect. A **824**, 598–599 (2016).
8. J. C. Driggers, "Improving astrophysical parameter estimation via offline noise subtraction for advanced ligo," Phys. Rev. D **99**(4), 042001 (2019).
9. K. Goda, D. Ottaway, B. Connelly, R. Adhikari, N. Mavalvala, and A. Gretarsson, "Frequency-resolving spatiotemporal wave-front sensor," Opt. Lett. **29**(13), 1452–1454 (2004).
10. A. M. Gretarsson, E. D'Ambrosio, V. Frolov, B. O'Reilly, and P. K. Fritschel, "Effects of mode degeneracy in the ligo livingston observatory recycling cavity," J. Opt. Soc. Am. B **24**(11), 2821–2828 (2007).
11. J. Betzweiser, "Analysis of spatial mode sensitivity of a gravitational wave interferometer and a targeted search for gravitational radiation from the crab pulsar," Ph.D. thesis, Massachusetts Institute of Technology, Cambridge, Masschusetts (2007).
12. K. Agatsuma, L. van der Schaaf, M. van Beuzekom, D. Rabeling, and J. van den Brand, "High-performance phase camera as a frequency selective laser wavefront sensor for gravitational wave detectors," Opt. Express **27**(13), 18533–18548 (2019).
13. D. V. Martynov, "Sensitivity of the advanced ligo detectors at the beginning of gravitational wave astronomy," Phys. Rev. D **93**(11), 112004 (2016).
14. D. J. Ottaway, P. Fritschel, and S. J. Waldman, "Impact of upconverted scattered light on advanced interferometric gravitational wave detectors," Opt. Express **20**(8), 8329–8336 (2012).
15. M. Tacca, "Phase camera realignment," Virgo Observatory electronic logbook entry 45289 (2019).
16. S. J. Waldman, "The enhanced LIGO output mode cleaner," Technical report T080144, LIGO Scientific Collaboration (2009).
17. K. Arai, "On the accumulated round-trip gouy phase for general optical cavity," Technical report T1300189, LIGO Scientific Collaboration (2013).
18. D. D. Brown and A. Freise, "Finesse," (2014). You can download the binaries and source code at http://www.gwoptics.org/finesse.
19. S. Nayar and V. Branzoi, "Adaptive dynamic range imaging: optical control of pixel exposures over space and time," in *Proceedings Ninth IEEE International Conference on Computer Vision*, (2003), pp. 1168–1175 vol.2.
20. Y. Zhongdong, W. Peng, L. Xiaohui, and S. Changku, "3d laser scanner system using high dynamic range imaging," Opt. Lasers Eng. **54**, 31–41 (2014).
21. H. Mannami, R. Sagawa, Y. Mukaigawa, T. Echigo, and Y. Yagi, "Adaptive dynamic range camera with reflective liquid crystal," J. Vis. Commun. Image Represent. **18**(5), 359–365 (2007).
22. "Initial analysis of optical lock-in camera data at lho," https://alog.ligo-wa.caltech.edu/aLOG/index.php?callRep=52945.
23. "Reducing backscatter issues at pop port with the phase camera," https://alog.ligo-wa.caltech.edu/aLOG/index.php?callRep=52759.